# Plasmonics: a path towards HOT infrared detectors

*Original*

Plasmonics: a path towards HOT infrared detectors / Vallone, M., Goano, M., Hanna, S., Figgemeier, H., Eich, D., Bertazzi, F., Tibaldi, A.. - ELETTRONICO. - 13360:(2025), pp. 1-11. (SPIE Photonics West - OPTO San Francisco (USA) 25-30 gennaio 2025) [10.1117/12.3040145].

*Publisher:*
SPIE

*Published*
DOI:10.1117/12.3040145

# Plasmonics: a path towards HOT infrared detectors

Marco Vallone[1], Michele Goano[1,2], Stefan Hanna[3], Heinrich Figgemeier[3], Detlef Eich[3],
Francesco Bertazzi[1], and Alberto Tibaldi[1]

[1]Dipartimento di Elettronica e Telecomunicazioni, Politecnico di Torino, corso Duca degli Abruzzi 24, 10129 Torino, Italy
[2]IEIIT-CNR, corso Duca degli Abruzzi 24, 10129 Torino, Italy
[3]AIM Infrarot-Module GmbH, Theresienstraße 2, 74072 Heilbronn, Germany

## ABSTRACT

Increasing the operating temperature while enhancing the detectivity $D^*$ is paramount for the advancement of HgCdTe infrared detectors. We present multiphysics TCAD simulations demonstrating how plasmonic resonances can enable submicron-thick HgCdTe absorbers to operate up to 260 K in the mid-infrared band (MWIR, $\lambda \in [3,5]\,\mu\text{m}$), promising $D^*$ more than twofold compared to those provided by conventional 5 µm-thick absorbers, with comparable responsivity. Different nanostructured surfaces are presented as solutions suitable for either covering the entire MWIR, or for narrow-band detectors.

**Keywords:** plasmonic cavities, HgCdTe photodetectors, infrared detectors, multiphysics TCAD simulations

## 1. INTRODUCTION

The infrared (IR) detectors industry is striving towards the improvement of the responsivity of focal plane array (FPA) detectors[1] by fostering the coupling of light to the absorbing material through nanostructured surfaces[2,3] or plasmonic structures,[4–9] where surface plasmon polaritons (SPPs) can be exploited to this purpose. SPPs are optical modes that can propagate at metallic-dielectric interfaces, where collective surface excitations of free electrons are coupled to evanescent electromagnetic fields in the dielectric.[10,11]

IR detectors integrated in plasmonic cavities could represent an alternative to more mature high operating temperature (HOT) infrared photodetectors designs,[12–14] presently represented by $n$B$n$ barrier detectors[15–22] or fully-depleted double-layer planar heterostructures (DLPH).[23–28] Although theoretically successful, these strategies exhibit some realization problems. For example, DLPH detectors require extremely low residual doping in the absorber,[24,25,27] while barrier detectors require very abrupt composition and doping profiles[20,29,30] to be obtained with careful calibration of the annealing time during fabrication,[18] to avoid negative effects on the dark current. Moreover, the reduction of the valence band barrier[31] is necessary to favor the flow and collection of the photogenerated minority carriers and is not a trivial issue. To this end, superlattice-based barriers[22,31,32] or $p$B$n$ profiles with acceptor doped barriers are often considered and, in the latter case, a $n^+p^+$ tunnel-junction is often required[30] to improve the electrical $p$-contact, increasing fabrication complexity.

The high versatility of II-VI $\text{Hg}_{1-x}\text{Cd}_x\text{Te}$ (mercury cadmium telluride, MCT) alloys already allows for the fabrication of IR detectors featuring high absorption properties, hence high responsivity, provided the absorber thickness $t_{\text{abs}}$ is in the order of (or a little larger than) the operating wavelength. For the mid-infrared band (MWIR, $\lambda \in [3,5]\,\mu\text{m}$), this makes $t_{\text{abs}} \approx 5\,\mu\text{m}$ a good compromise. However, since in MCT the dark current increases rapidly with increasing temperature,[1] a possible solution is to exploit SPPs to develop a plasmonic IR photodetector characterized by a very thin (submicron) absorber. This makes it possible to reduce the dark current $I_{\text{dark}}$ and increase the specific detectivity $D^*$[16]

$$D^* \approx \frac{S^{1/2}\mathcal{R}}{\sqrt{2\,\mathrm{e}\,I_{\text{dark}}}}, \tag{1}$$

---

Send correspondence to M. Goano, E-mail: michele.goano@polito.it

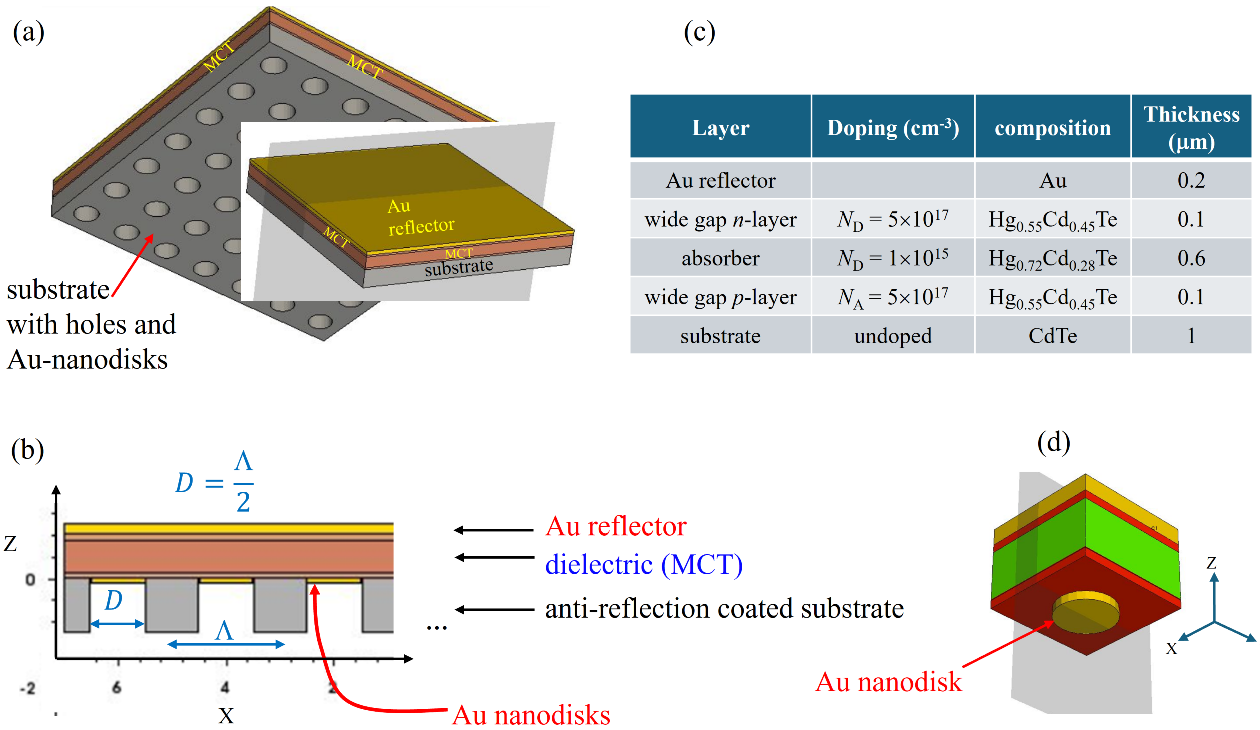

| Layer | Doping (cm$^{-3}$) | composition | Thickness (μm) |
|---|---|---|---|
| Au reflector | | Au | 0.2 |
| wide gap *n*-layer | $N_D = 5\times10^{17}$ | $Hg_{0.55}Cd_{0.45}Te$ | 0.1 |
| absorber | $N_D = 1\times10^{15}$ | $Hg_{0.72}Cd_{0.28}Te$ | 0.6 |
| wide gap *p*-layer | $N_A = 5\times10^{17}$ | $Hg_{0.55}Cd_{0.45}Te$ | 0.1 |
| substrate | undoped | CdTe | 1 |

Figure 1. (a) The plasmonic cavity with (b) its 2D section, showing a 2D Λ-periodic nanoarray of holes and Au nanodisks. In the table (c), the detail of the epitaxial layers, and in (d) the elementary cell needed for simulations, where periodic boundary conditions are imposed on the $\hat{x}$, $\hat{y}$ directions. Reprinted with permission from[33] © Optica Publishing Group.

since in most cases $I_{\text{dark}} \propto t_{\text{abs}}$.[21] Here e is the elementary charge, $S$ is the illuminated area of the detector and $\mathcal{R}$ is the responsivity, which is defined as

$$\mathcal{R} = \frac{J_{\text{ph}}}{P}, \tag{2}$$

where $P$ is the optical power density and $J_{\text{ph}} = J - J_{\text{dark}}$ is the photocurrent density, where $J$ and $J_{\text{dark}}$ are the current density under illumination and in dark, respectively. The excitation of plasmonic resonances at suitable wavelengths can increase the responsivity $\mathcal{R}$ and thus compensate for its reduction due to the use of a thinner absorber than usual. In Section 2 we present the working principle of this type of detectors, while in Section 3 we describe the simulation framework. As a reference case study, in Section 4 we describe an introductory example consisting of a very simple plasmonic cavity.[33] Despite its basic structure, it is sufficient to recognize the possibilities of the idea and to stimulate new developments. An example of this is Section 5, where we propose an interesting alternative. Section 6 summarizes the most important results.

## 2. PLASMONIC RESONANCES TO ENHANCE DETECTIVITY

Aiming to overcome the trade-off between responsivity and dark current towards HOT detectors, it is possible to employ SPPs to enable a reduction of $t_{\text{abs}}$ (therefore, of the dark current) without introducing a significant penalty on $\mathcal{R}$, enhancing $D^*$ by an increase of $J_{\text{ph}}$ for given $P$.

In this view, the starting point of our analysis is the single pixel shown in Fig. 1, which consists of a CdTe substrate on which a HgCdTe-based heterostructure is epitaxially grown with the doping and composition profiles detailed in the table reported in panel (c), followed by a 0.2 µm-thick Au reflector. Concerning the fabrication, appropriate lithographic and etching techniques (*e.g.,* electron-beam lithography) can be employed to obtain a Λ-periodic series of nanoholes on the substrate, where, by sputtering, 50 nm-thick gold nanodisks with diameter $D = \Lambda/2$ can be deposited on their bottom (see a discussion concerning this choice for $D$ in [34, Fig. 3(a)]).

The optical field profile in this device results from the hybridization of two mode families, the optical cavity (OC) and the SPP modes, which are described hereafter.

## OC modes

When the detector is illuminated from below, the round-trip phase-shift condition[35]

$$n_{\mathrm{MCT}}\, t_{\mathrm{abs}} = \left(m + \frac{1}{2}\right) \frac{\lambda_m}{2}, \quad m = 0, 1, ... \tag{3}$$

determines the maximum absorption for optical cavity modes with wavelength $\lambda_m$.

## SPP modes

SPPs are surface collective excitations of free electrons that can propagate along a metal-dielectric interface, satisfying the dispersion relation

$$k_x = \frac{2\pi}{\lambda} n_{\mathrm{eff}} \tag{4}$$

where

$$n_{\mathrm{eff}} = \Re \sqrt{\frac{\epsilon_{\mathrm{Au}} \epsilon_{\mathrm{MCT}}}{\epsilon_{\mathrm{Au}} + \epsilon_{\mathrm{MCT}}}} \tag{5}$$

($\Re$ indicates the real part). Here, $\epsilon_{\mathrm{Au}}$ and $\epsilon_{\mathrm{MCT}}$ are the complex dielectric functions of gold and MCT, respectively, and Eq. (4) implicitly indicates that the SPP is propagating along $\hat{x}$[10, 11] (see the axes orientation in Fig. 1). However, for normal incidence along $\hat{z}$, the boundary conditions of Maxwell's equations enforce the continuity of the transverse wavevector components, *i.e.,* $k_x = 0$, which prevents the possibility to excite a SPP mode. Nevertheless, the 2D nanodisks array with period $\Lambda$ provides efficient optical scattering for wavevector[6, 7, 36]

$$\mathbf{K}_{p,q} = \frac{2\pi}{\Lambda} \left(\sin(\theta)\, \hat{u} \pm p\, \hat{x} \pm q\, \hat{y}\right), \quad p,\, q = 0, 1, ... \tag{6}$$

where $\hat{u}$ is a unit vector in the direction of the in-plane component of the incident light wavevector $\mathbf{k}$, and we assumed that the reciprocal lattice vectors are parallel to the unit vectors $\hat{x}$ and $\hat{y}$. Based on this idea, by equating $k_x$ in Eq. (4) to $|\mathbf{K}_{p,q}|$ for normal incidence ($\theta = 0$), we obtain the condition

$$\lambda_{\mathrm{SPP},p,q} = \frac{\Lambda}{\sqrt{p^2 + q^2}} n_{\mathrm{eff}}, \tag{7}$$

which defines the wavelength of the impinging plane wave that excites the SPP modes.

### 2.1 Spectral response of the cavity

The spectral responsivity $\mathcal{R}(\lambda)$ of the photodetector results from the typical bulk-like absorption contribution (Lambert-Beer law [37, Sec. 4.11.2]), and the OC and SPP discrete spectral resonances, whose peaks are determined by the discrete spectrum of the plasmonic cavity Hamiltonian $\hat{H}$. Depending on the selected design, the absorption efficiency, and thus the responsivity and detectivity of the photodetector, can be significantly increased at the wavelengths corresponding to the eigenvalues of $\hat{H}$. They correspond neither to purely-OC nor to purely-SPP modes, but to the so-called *hybrid modes* determined by their interaction, and it is of central importance to calculate their spectral features.

The Hamiltonian $\hat{H}$, when expressed in the occupation number formalism defined later, reads[33]

$$\begin{aligned} \hat{H} = & E_{\mathrm{OC},m}\, \hat{a}^\dagger \hat{a} + E_{\mathrm{SPP},p,q}\, \hat{b}^\dagger \hat{b} \\ & + \mathrm{i}\gamma \left(\hat{a}^\dagger - \hat{a}\right) \left(\hat{b}^\dagger + \hat{b}\right) + \delta \left(\hat{b}^\dagger + \hat{b}\right)^2 \end{aligned} \tag{8}$$

where $E_{\mathrm{OC},m}$ and $E_{\mathrm{SPP},p,q}$ are the OC and SPP energies corresponding to $\lambda_m$ and $\lambda_{\mathrm{SPP},p,q}$ provided by Eq. (3) and Eq. (7), respectively. Moreover, $\gamma$ and $\delta$ are the SPP-OC interaction energy and the SPP-SPP dipole-interaction energy, respectively, $\hat{a}^\dagger$ ($\hat{a}$) is the creation (annihilation) photon operator and $\hat{b}^\dagger$ ($\hat{b}$) are similar operators for plasmons. Within this formalism (see an extended description in[33]), the spectral resonances have energies $E_\pm$ which follow from the diagonalization of $\hat{H}$ as

$$\begin{aligned}E_\pm^2 = {} & \frac{E_{\mathrm{OC},m}^2 + E_{\mathrm{SPP},p,q}^2 + 2E_{\mathrm{SPP},p,q}\,\delta}{2} \\ & \pm \frac{1}{2}\left\{\left[E_{\mathrm{OC},m}^2 - \left(E_{\mathrm{SPP},p,q}^2 + 2E_{\mathrm{SPP},p,q}\,\delta\right)\right]^2\right. \\ & \left. +16\gamma^2 E_{\mathrm{SPP},p,q}E_{\mathrm{OC},m}\right\}^{1/2}, \qquad (9)\end{aligned}$$

which correspond the wavelengths $\lambda_\pm$, known in the literature as hybrid "upper" and "lower" SPP-OC modes.

Eq. (9) reliably determines the spectral position of the resonances $\lambda_\pm$ as a function of the cavity parameters ($\Lambda$, $t_{\mathrm{abs}}$, $n_{\mathrm{eff}}$, etc.) only if the geometry of the cavity is so simple and symmetric that estimates of $E_{\mathrm{OC},m}$ and $E_{\mathrm{SPP},p,q}$ are possible through the simple models represented by Eqs. (3)–(7). In most cases, the accurate spectral position of the hybrid modes require full-wave electromagnetic numerical simulations, although the analytical models represented by Eq. (9) are important as a guideline and for understanding the results and engineering the design. Moreover, numerical simulations are essential to solve the carrier transport problem to provide realistic spectra of the responsivity $\mathcal{R}$ and the detectivity $D^*$, which are figures of merit obtained through typical experimental characterizations. In this perspective, Section 3 describes the adopted numerical simulation framework. It consists of solving the Maxwell equations for the optical problem, and the Poisson and continuity equations for studying the transport of electrons and holes. The simulation procedure provides $\mathcal{R}$ and $D^*$ in the plane $(\Lambda, \lambda)$ according to (2) and (1) for the structure in Fig. 1, where the resonances $\lambda_\pm$ approximately in accordance with Eq. (9) are expected to be clearly visible.

## 3. METHODS

The three-dimensional (3D) multiphysics model we employed integrates the Synopsys RSoft FullWAVE tool,[38] which solves the electromagnetic problems with a finite-difference time-domain (FDTD) approach. The electromagnetic problem is solved assuming a fine discretization ($\approx \lambda/30$) and a monochromatic plane-wave illumination with propagation vector along the $\hat{z}$ direction, whose electric field exhibits the time-harmonic form $\mathbf{E} = E_0 \exp(\mathbf{k}\cdot\mathbf{r} - \omega t)$ and is oriented along the $\hat{x}$ direction. Moreover, $E_0$ is specified in terms of the input power density $P$, and all the detector variants described throughout the present work have their illuminated face in the $(x, y)$ plane. As a result, the FDTD solver provides the spatially-resolved electromagnetic field, from which it is possible to evaluate the absorbed photon density $A_{\mathrm{opt}}$ as the divergence of the time-averaged Poynting vector $\vec{S}$ [39, Sec. 6.8][37,40–44]

$$A_{\mathrm{opt}}(\lambda, \mathbf{r}) = -\frac{\vec{\nabla}\cdot\langle\vec{S}(\lambda)\rangle}{hc/\lambda}, \qquad (10)$$

where $\mathbf{r}$ is the vector position. The spatial distribution of $A_{\mathrm{opt}}$ provides one of the most interesting figures of merit, the spectral absorption efficiency

$$\eta(\lambda) = \frac{hc}{\lambda P}\int_V A_{\mathrm{opt}}(\lambda, \mathbf{r})\,\mathrm{d}^3\mathbf{r} \qquad (11)$$

($h$ and c are the Planck constant and the light velocity in vacuum, and $V$ is the absorber volume), which can be employed still before any carriers transport simulation to have an idea of the detector optical response and to select the most promising design solutions.

RSoft includes realistic models of the complex refractive index $\hat{n}$ of the alloys under investigation, taking into account wavelength and temperature effects. Specifically, $\hat{n}$ for gold and for MCT are evaluated from the respective relative complex dielectric functions $\epsilon_{\mathrm{Au}}$ and $\epsilon_{\mathrm{MCT}}$. For $\epsilon_{\mathrm{MCT}}$ we adopted the model described in[45] and [46, Sec. 9.6]. Regarding $\epsilon_{\mathrm{Au}}$, we adopted the Drude form in,[47]

$$\epsilon_{\mathrm{Au}}(\omega) = \epsilon_\infty - \frac{\omega_p^2}{\omega^2 - i\omega\omega_t}, \qquad (12)$$

where $\epsilon_\infty = 1$, $\omega_p = 1.37 \times 10^{16}$ rad/s, and $\omega_t = 4.65 \times 10^{13}$ rad/s.

Periodic boundary conditions (PBCs) along $\hat{x}$ and $\hat{y}$, and convolutional perfectly matched layer (CPML) absorbing BCs[48] along $\hat{z}$, allow to take advantage of the $\Lambda$-periodicity of the structure shown in Fig. 1 to simulate just an elementary cell (panel (d)), obtaining results which are representative of an entire pixel[34] with much lower computational effort.

The modeling of the electromagnetic response can be followed by carrier transport simulations to assess $J_{\text{dark}}$ and, under illumination, $J_{\text{ph}}$, $\mathcal{R}$ and $D^*$. This is achieved by employing the commercial simulation suite Sentaurus Device by Synopsys,[49] which discretizes the Poisson-drift-diffusion system in 3D using a stabilized finite-box method,[44,50] where the optical generation rate evaluated from $A_{\text{opt}}$ is incorporated as a source term in the continuity equations, which also include Shockley-Read-Hall (SRH) and Auger generation-recombination (GR) processes, modeled as in[51] and,[52] respectively. To determine the carrier density, Fermi-Dirac statistics are used, also accounting for incomplete ionization of doping densities. Moreover, all the adopted models concerning the material parameters and carriers generation-recombination mechanisms are detailed in Table S1, Supplement 1 of.[33]

The SRH lifetime $\tau_{\text{SRH}}$ is only related to the material defect density and carrier trapping cross sections,[51] and thus it may be considered a technology-dependent parameter. We use for $\tau_{\text{SRH}}$ a value of 10 µs, which is representative, for MCT, of average-quality materials.[25,31] Auger lifetime $\tau_{\text{Aug}}$ is not related to the material quality, as it depends only on the MCT Cd mole fraction, temperature, and doping density [33, Table S1]. In particular, $\tau_{\text{Aug}}$ decreases rapidly for increasing temperature, corresponding to a steep increase of $J_{\text{dark}}$. Since $J_{\text{dark}}$ depends mainly on lifetimes $\tau_{\text{SRH}}$ and $\tau_{\text{Aug}}$ and from the absorber thickness $t_{\text{abs}}$ (see, *e.g.,*[21,31,53] for an extended discussion about this point), the opportunity to reduce $t_{\text{abs}}$ without penalizing $\mathcal{R}$ could make thin, plasmonic MCT detectors as a possible solution to enable high operating temperatures.

It should be emphasized that detectors generally have an anti-reflective coating (ARC) deposited on their illuminated face, which is very difficult to include in the simulation setup. We solved this problem by defining the illumination source reference plane just inside the substrate, as shown in Fig. 1(b). This approach allows not only for a more realistic estimate of $\mathcal{R}$, but also for a significant reduction of the optical cavity effect (*i.e.*, the OC resonance), as expected in fabricated devices including a well-designed ARC.

## 4. STARTING POINT: GOLD REFLECTOR AND 2D ARRAY OF NANODISKS

As an example of calculation extensively discussed in[33] and here briefly recalled, it is interesting to compare the considered plasmonic, 0.8 µm-thick detector with a standard (*i.e.*, non-plasmonic) one with absorber thickness $t_{\text{abs}} = 5$ µm. Considering the two elementary cells and the contact scheme shown in Fig. 2(a), PBCs have been applied along $\hat{x}$, $\hat{y}$ and CPMLs along $\hat{z}$. We emphasize that the plasmonic detector includes both the gold reflector and the $\Lambda$-periodic 2D array of nanodisks (NDs) as shown in Fig. 1 and Fig. 2(a), while the standard, much thicker detector only includes the gold reflector. For the sake of brevity, they are referred to as ND-PLASM and SD (*i.e.*, standard detector), respectively.

We have performed an electromagnetic FDTD parametric simulation campaign varying $\lambda$ and $\Lambda$, each followed by a simulation of the carrier transport problem, which yields the dark current, the photocurrent, the responsivity $\mathcal{R}$ and the spectral specific detectivity $D^*$. In the carrier transport simulation, the bias contact is defined on the pixel nanodisks, which are deposited on the $n$-doped HgCdTe layer with wider band-gap, and the ground contact is connected to the reflector as shown in Fig. 2(a) for the elementary cell. The electrical simulations have been performed by operating the detector in reverse bias to $V_{\text{bias}} = -0.5$ V, in the dark and under illumination, for $\Lambda \in [0.3, 2.4]$ µm, and in the waveband $\lambda \in [0.25, 5.5]$ µm.

Fig. 2(b) shows the obtained 2D color map of $\mathcal{R}$ at $T = 160$ K for the ND-PLASM detector, where we have also included the fundamental SPP mode $\lambda_{\text{SPP}}$ with a black solid line. The "upper" and "lower" modes are clearly visible, and they arise from the interaction between the SPP mode $\lambda_{\text{SPP}}$ and the OC mode at $\lambda_{\text{m}} \approx 5$ µm, not shown in the figure.

To obtain more quantitative results, we compared the properties of the SD with the ND-PLASM adopting for the latter $\Lambda = 1.3$ µm and $\Lambda = 1.8$ µm. In Fig. 2(c,d) the spectral responsivity $\mathcal{R}$ and detectivity $D^*$ are

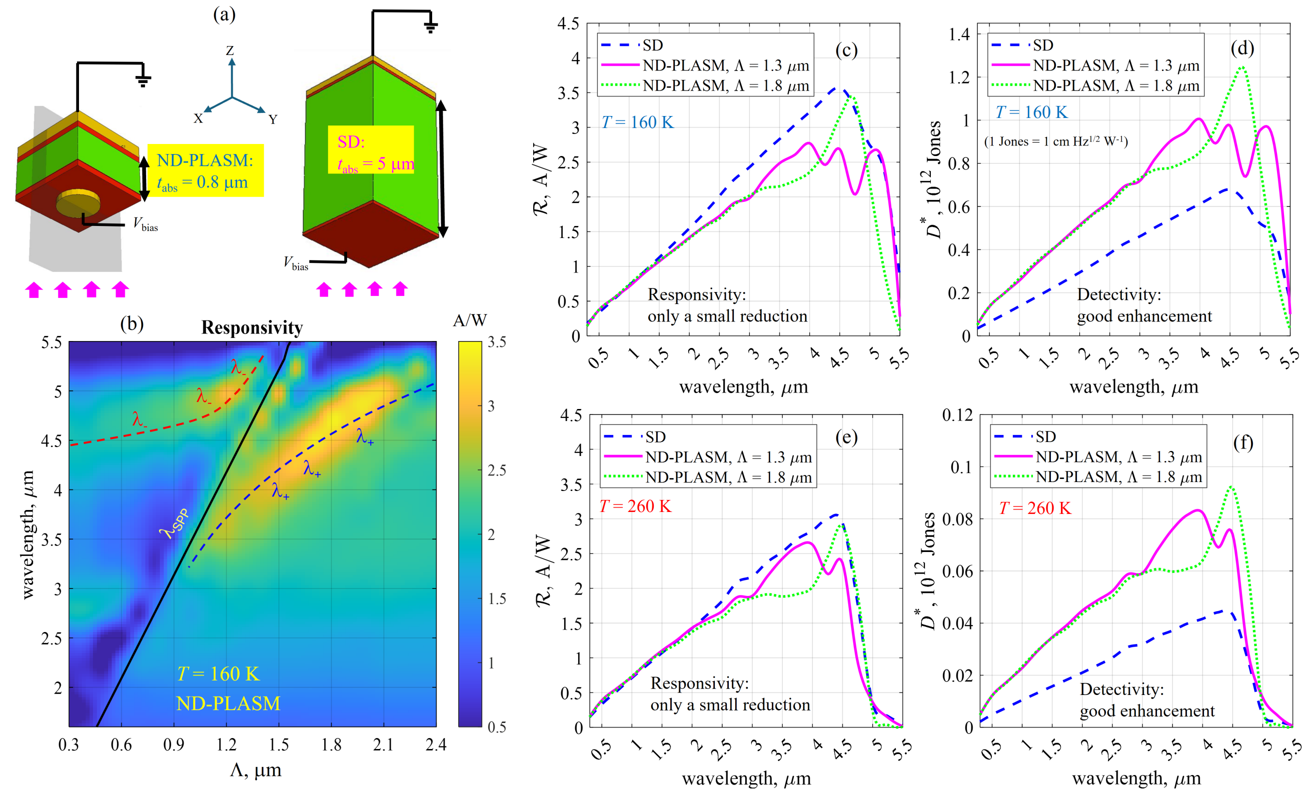

Figure 2. (a) Electrical contacting strategy, with a scheme of the elementary cell of the plasmonic and standard detectors. (b) Color map of the responsivity in the $(\Lambda, \lambda)$ parameter space at $T = 160\,\mathrm{K}$. The "lower" and "upper" hybrid plasmon resonances are well visible and marked as $\lambda_-$ and $\lambda_+$, respectively. The solid black oblique line is the $\lambda_{\mathrm{SPP}}$ mode. (c) $\mathcal{R}$ and (d) $D^*$ spectra at $T = 160\,\mathrm{K}$ for the standard and the plasmonic detectors, considering for the latter $\Lambda = 1.3\,\mu\mathrm{m}$ and $\Lambda = 1.8\,\mu\mathrm{m}$. In panels (e) and (f), the same results refer to the temperature $T = 260\,\mathrm{K}$.

reported for the two structures at $T = 160\,\mathrm{K}$, and for $T = 260\,\mathrm{K}$ in Fig. 2(e,f). Since the plasmonic detector is much thinner than the standard one, its dark current is lower by a factor of $\approx 3$ at $T = 160\,\mathrm{K}$ and by a factor of $\approx 4.6$ at $T = 260\,\mathrm{K}$ at the operating reverse bias, making $D^*$ to increase by the square root of the same factor according to Eq. (1), since $\mathcal{R}$ for the plasmonic detector is only slightly penalized around the peak.

## 5. ALTERNATIVE: 2D ARRAY OF CROSS-SHAPED GOLD NANORODS

Different shapes of nanoparticles employed as elements of 2D gratings are expected to have different effects on plasmonic detectors. A 2D lattice of parallel nanorods is expected to be very sensitive to the polarization of the electromagnetic radiation incident on the active surface, exhibiting a maximum absorption efficiency when the polarization vector is parallel to the nanorods. They can be of interest when high polarization sensitivity is targeted.

Cross-shaped nanorods could have a different behavior, which makes their analysis very interesting. Inspired by preliminary results from the literature[54] that, however, do not include transport simulations required to estimate $\mathcal{R}$ and $D^*$, we considered a 2D array of cross-shaped gold nanorods located on the illuminated side of the photodetector, and the same gold reflector as in Section 4.

By applying PBCs along $\hat{x}$, $\hat{y}$ and CPMLs along $\hat{z}$, the same $\Lambda \times \Lambda$ unit cell as the reference structure described in Fig. 2(a) can be considered, except that the nanodisk is replaced by a cross-shaped nanorod, as we show in Fig. 3(a). In what follows we refer to this type of plasmonic device as X-PLASM. The absorber is unchanged with respect to the reference structure, in particular its thickness is $0.8\,\mu\mathrm{m}$, and all comparisons are made with respect to the same SD already considered in Section 4, whose thickness is $5\,\mu\mathrm{m}$. Concerning the X-PLASM,

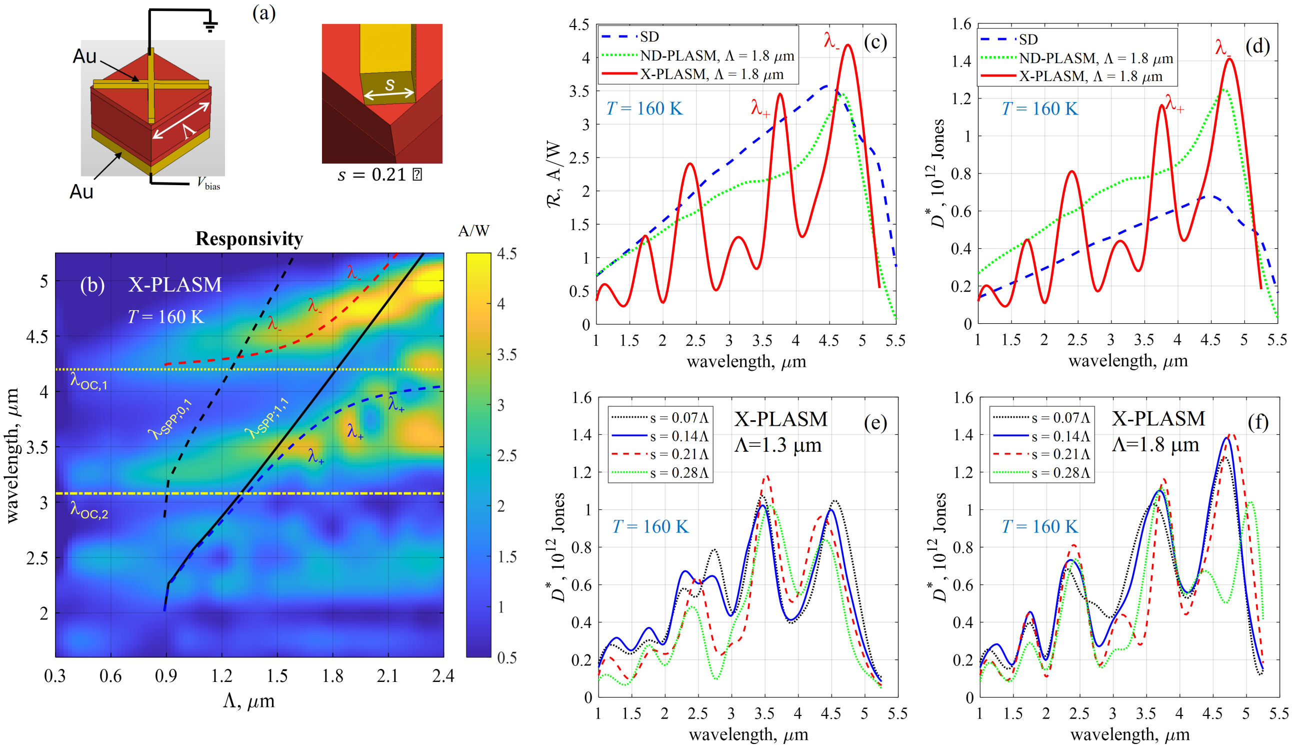

Figure 3. (a) Schematics of the X-PLASM detector, with the color map (b) of its responsivity for $s = 0.21\Lambda$ in the domain $(\Lambda, \lambda)$. Comparison of the responsivity (c) and detectivity (d) between the SD, and the ND-PLASM and X-PLASM detectors for $\Lambda = 1.8\,\mu$m. Effects of the nanorods thickness $s$ on $D^*$ for the X-PLASM detector with $\Lambda = 1.3\,\mu$m (e) and $\Lambda = 1.8\,\mu$m (f).

the nanorod thickness $s$ is particularly important, which is defined as a fraction of the 2D period $\Lambda$, while the nanorods occupy all the elementary cell.

As a starting point, we have chosen $s = 0.21\Lambda$ and performed combined electromagnetic FDTD and carrier transport simulations for each $\lambda$- and $\Lambda$-point at $T = 160\,$K, whose results are summarized in the color map of $\mathcal{R}$ shown in Fig. 3(b). The two black slanted lines are the SPP modes $\lambda_{\text{SPP};0,1}$ (dashed line) and $\lambda_{\text{SPP};1,1}$ (solid line). The polarization vector of the illuminating electromagnetic field forms an angle of 45° to both the nanorods, consequently the order of the SPP mode which matters in the SPP-OC hybridization is not the fundamental one ($\lambda_{\text{SPP};0,1}$ or $\lambda_{\text{SPP};1,0}$), but the first symmetric mode $\lambda_{\text{SPP};1,1}$, and the resonances of the "upper" and "lower" hybrid modes are clearly visible.

A limitation of the analytical model that provides $\lambda_{\text{SPP}}$ (and in turn the $E_{\text{SPP}}$ which enters in Eq. (9)) is the lack of an explicit relation between $n_{\text{eff}}$, $\Lambda$ and the presence of a nanoparticle of given shape close to the reflector-absorber interface. Eq. (7) results to be a rough approximation, and the FDTD numerical simulations clearly indicate that $\lambda_{\text{SPP};1,1}$ increases less than linearly with $\Lambda$, suggesting that $n_{\text{eff}}$ should decrease for increasing $\Lambda$.

To obtain more quantitative results, we considered a comparison between the SD, the X-PLASM, and the ND-PLASM detector described in Section 4 and in more detail in.[33] Fig. 3(c,d) compares the responsivity $\mathcal{R}$ and the detectivity $D^*$ for the three kinds of detectors, having chosen for the plasmonic ones an intermediate value for the lattice period, $\Lambda = 1.8\,\mu$m. Concerning the X-PLASM detector, it is possible to notice several, quite well-defined resonances, leading to a strongly non-monotonic wavelength dependence of responsivity and detectivity. In this view, the resulting photodetectors are not very suited for broad-band detection. On the other hand, considering that the maxima are sufficiently large and very high, such devices are potentially very interesting for narrow-band detection.

The effects of changing the thickness $s$ are clearly visible in Fig. 3(e,f), respectively for $\Lambda = 1.3\,\mu$m and

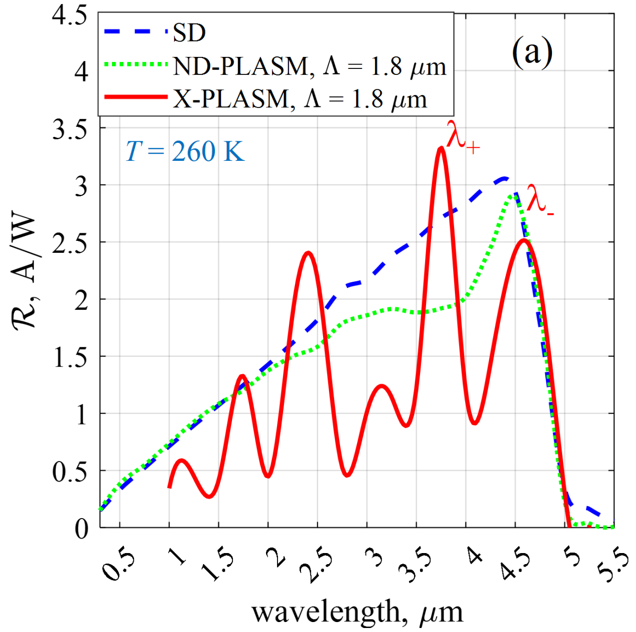

Figure 4. Responsivity (a) and detectivity (b) at $T = 260\,\mathrm{K}$ for the SD, the ND-PLASM and X-PLASM detectors. For the two plasmonic solutions we selected $\Lambda = 1.8\,\mu\mathrm{m}$.

$\Lambda = 1.8\,\mu\mathrm{m}$. In the latter case, the maximum detectivity is expected for $s$ between $0.15\Lambda$ and $0.20\Lambda$. Below these values, the SPP resonances start weakening, while above them the nanorods maybe cover too much the elementary cell. For $\Lambda = 1.3\,\mu\mathrm{m}$, all the four cases perform quite well.

It is to be remarked that the primary goal of this investigation is the achievement of HOT operation by exploiting plasmonics. Therefore we repeated the same simulation campaign setting $T = 260\,\mathrm{K}$, a temperature which can be achieved without expensive cooling equipments. Fig. 4 shows an example of results, obtained for $\Lambda = 1.8\,\mu\mathrm{m}$. Here we compare the $\mathcal{R}$ and $D^*$ for the SD, the ND-PLASM, and the X-PLASM photodetectors at $T = 260\,\mathrm{K}$. Since $\mathcal{R}$ for the X-PLASM detector is quite high around the resonance $\lambda_+$ (since the temperature-induced blue-shift reduced the resonance $\lambda_-$), the corresponding specific detectivity $D^*$ increases significantly with respect to both the thick SD and the ND-PLASM, indicating the potential interest for this type of plasmonic detector.

## 6. CONCLUSIONS

The motivation behind the investigation of plasmonic cavities in MCT detectors is to pave the way towards the fabrication of IR detectors with reduced dark current and improved detectivity, hence simplifying cooling systems, thanks to the possibility to employ submicron-thick absorbers introducing no penality on the responsivity $\mathcal{R}$.

Multiphysics TCAD simulations show that appropriately tuned plasmonic resonances compensate for the reduction in absorption which results from the use of a very thin absorber layer. The net effect is the achievement of a responsivity which is only slightly lower than in standard detectors with a thickness of $5\,\mu\mathrm{m}$. The final result is a specific detectivity that exceeds the corresponding standard detector $D^*$ by a factor of $\approx 2$ around the spectral peak. These properties hold even at $T = 260$ K, which could enable using Peltier cells in place of the presently required very complex and expensive cryocoolers.

The presence of the SPP-OC interactions splits the plasmonic mode into two hybrid modes, leading to the ”upper” and ”lower” hybrid resonances. By nanostructuring the illuminated side of the detector in different ways, it is possible either to broaden the optical spectral response as described in Section 4, offering the chance to cover the entire MWIR band with a single detector, or to obtain more wavelength selective optical response, as shown in Section 5.

Additionally, when the detector is thin, it is possible to extract carriers quickly, since the carriers transit time is determined by the absorber thickness.[55] Consequently, a higher frequency response is achieved, which could be an important characteristic in many high-speed applications.

## ACKNOWLEDGMENTS

This work was supported in part by the European Union under two initiatives of the Italian National Recovery and Resilience Plan (NRRP) of NextGenerationEU: the partnership on *Telecommunications of the Future* (PE00000001 – program "RESTART"), and the National Centre for HPC, Big Data and Quantum Computing (CN00000013 – CUP E13C22000990001).

## REFERENCES

[1] Rogalski, A., [*Infrared Detectors*], CRC Press, Boca Raton, FL, 2nd ed. (2011).

[2] Wehner, J. G. A., Smith, E. P. G., Venzor, G. M., Smith, K. D., Ramirez, A. M., Kolasa, B. P., Olsson, K. R., and Vilela, M. F., "HgCdTe photon trapping structure for broadband mid-wavelength infrared absorption," *J. Electron. Mater.* **40**(8), 1840–1846 (2011).

[3] Schuster, J. and Bellotti, E., "Analysis of optical and electrical crosstalk in small pitch photon trapping HgCdTe pixel arrays," *Appl. Phys. Lett.* **101**(26), 261118 (2012).

[4] Rosenberg, J., Shenoi, R. V., Krishna, S., and Painter, O., "Design of plasmonic photonic crystal resonant cavities for polarization sensitive infrared photodetectors," *Opt. Express* **18**(4), 3672–3686 (2010).

[5] Tong, J., Tobing, L. Y. M., Qiu, S., Zhang, D. H., and Perera, A. G. U., "Room temperature plasmon-enhanced $InAs_{0.91}Sb_{0.09}$-based heterojunction *n-i-p* mid-wave infrared photodetector," *Appl. Phys. Lett.* **113**(1), 011110 (2018).

[6] Tappura, K., "Enhancing the performance of commercial infrared detectors by surface plasmons," *MDPI Proc.* **2**(13), 1063 (2018).

[7] Vanamala, N., Santiago, K. C., and Das, N. C., "Enhanced MWIR absorption of HgCdTe (MCT) via plasmonic metal oxide nanostructures," *AIP Adv.* **9**, 025113 (2019).

[8] Budhu, J., Pfiester, N., Choi, K.-K., Young, S., Ball, C., Krishna, S., and Grbic, A., "Dielectric resonator antenna coupled antimonide-based detectors (DRACAD) for the infrared," *IEEE Trans. Antennas Propagation* (2021).

[9] Zhang, G., Xu, C., Sun, D., Wang, Q., Lu, G., and Gong, Q., "Metasurface-tuned light-matter interactions for high-performance photodetectors," *Fundam. Res. (in press)* (2024).

[10] Raether, H., [*Surface Plasmons on Smooth and Rough Surfaces and on Gratings*], vol. 111 of *Springer Tracts in Modern Physics*, Springer-Verlag, Berlin (1988).

[11] Han, Z. and Bozhevolnyi, S. I., "Radiation guiding with surface plasmon polaritons," *Rep. Prog. Phys.* **76**, 016402 (2013).

[12] Ashley, T. and Elliott, C. T., "Model for minority carrier lifetimes in doped HgCdTe," *Electron. Lett.* **21**(10), 451–452 (1985).

[13] Elliott, C. T., "Non-equilibrium modes of operation of narrow-gap semiconductor devices," *Semiconductor Sci. Technol.* **5**(35), S30 (1990).

[14] Martyniuk, P. and Rogalski, A., "HOT infrared photodetectors," *Opto-Electron. Rev.* **21**(2), 239–257 (2013).

[15] Maimon, S. and Wicks, G. W., "*nBn* detector, an infrared detector with reduced dark current and higher operating temperature," *Appl. Phys. Lett.* **89**(15), 151109 (2006).

[16] Itsuno, A. M., Phillips, J. D., and Velicu, S., "Predicted performance improvement of Auger-suppressed HgCdTe photodiodes and *p-n* heterojunction detectors," *IEEE Trans. Electron Devices* **58**, 501—507 (Feb. 2011).

[17] Itsuno, A. M., Phillips, J. D., and Velicu, S., "Mid-wave infrared HgCdTe nBn photodetector," *Appl. Phys. Lett.* **100**, 161102 (Apr. 2012).

[18] He, J., Wang, P., Li, Q., Wang, F., Gu, Y., Shen, C., Chen, L., Martyniuk, P., Rogalski, A., Chen, X., Lu, W., and Hu, W., "Enhanced performance of HgCdTe long-wavelength infrared photodetectors with nBn design," *IEEE Trans. Electron Devices* **67**, 2001–2007 (2020).

[19] Burlakov, I. D., Kulchitsky, N. A., Voitsekhovskii, A. V., Nesmelov, S. N., Dzyadukh, S. M., and Gorn, D. I., "Unipolar semiconductor barrier structures for infrared photodetector arrays (review)," *J. Commun. Technol. Electron.* **66**(9), 1084–1091 (2021).

[20] Voitsekhovskii, A. V., Dzyadukh, S. M., Gorn, D. I., Dvoretsky, S. A., Mikhailov, N. N., Sidorov, G. Y., and Yakushev, M. V., "Comprehensive experimental study of NB$\nu$N barrier structures based on n-HgCdTe MBE for detection in MWIR and LWIR spectra," *Phys. Scripta* **98**(6), 065907 (2023).

[21] Vallone, M., Alasio, M. G. C., Tibaldi, A., Bertazzi, F., Hanna, S., Wegmann, A., Eich, D., Figgemeier, H., Ghione, G., and Goano, M., "Exploring optimal dark current design in HgCdTe infrared barrier detectors: a TCAD and semianalytic investigation," *IEEE Photon. J.* **16**, 6800208 (Feb. 2024).

[22] Sellers, R., Sonde, S., Man, P., Khalidi, Z. E., Ahmad, Z., Velicu, S., and Zengeneh, D., "Fabrication and modeling study to reduce valence band offset in HgCdTe MWIR nBn photodetectors grown on silicon using superlattice barriers," in [*Infrared Sensors, Devices, and Applications XIII*], **PC12687, Proceedings of the SPIE**, PC1268709 (2023).

[23] Lei, W., Antoszewski, J., and Faraone, L., "Progress, challenges, and opportunities for HgCdTe infrared materials and detectors," *Appl. Phys. Rev.* **2**(4), 041303 (2015).

[24] Schuster, J., Tennant, W. E., Bellotti, E., and Wijewarnasuriya, P. S., "Analysis of the Auger recombination rate in $P^+N^-n^-N^-N$ HgCdTe detectors for HOT applications," in [*Infrared Technology and Applications XLII*], **9819, Proceedings of the SPIE**, 98191F (2016).

[25] Lee, D., Carmody, M., Piquette, E., Dreiske, P., Chen, A., Yulius, A., Edwall, D., Bhargava, S., Zandian, M., and Tennant, W., "High-operating temperature HgCdTe: A vision for the near future," *J. Electron. Mater.* **45**(9), 4587–4595 (2016).

[26] Schuster, J., DeWames, R. E., and Wijewarnasurya, P. S., "Dark currents in a fully-depleted LWIR HgCdTe $P$-on-$n$ heterojunction: analytical and numerical simulations," *J. Electron. Mater.* **46**(11), 6295–6305 (2017).

[27] Lee, D., Dreiske, P., Ellsworth, J., Cottier, R., Chen, A., Tallaricao, S., Yulius, A., Carmody, M., Piquette, E., Zandian, M., and Douglas, S., "Law 19: The ultimate photodiode performance metric," in [*Infrared Technology and Applications XLVI*], **11407, Proceedings of the SPIE**, 114070X, SPIE (2020).

[28] Rogalski, A., Martyniuk, P., Kopytko, M., and Hu, W., "Trends in performance limits of the HOT infrared photodetectors," *MDPI Appl. Sci.* **11**(2), 501 (2021).

[29] Alasio, M. G. C., Vallone, M., Molino, P., Errico, L., Hanna, S., Figgemeier, H., Tibaldi, A., Bertazzi, F., Ghione, G., and Goano, M., "Modeling the effects of graded and abrupt mole fraction profiles in pBn and nBn HgCdTe barrier detectors," in [*SPIE Optics+Photonics. Infrared Sensors, Devices, and Applications XIII*], **12687, Proceedings of the SPIE**, 126870E (Aug. 2023).

[30] Madejczyk, P., Gawron, W., Sobieski, J., Martyniuk, P., and Rutkowski, J., "MCT heterostructures for higher operating temperature infrared detectors designed in Poland," *Opto-Electron. Rev.* **31**, e144551 (2023).

[31] Martyniuk, P., Kopytko, M., and Rogalski, A., "Barrier infrared detectors," *Opto-Electron. Rev.* **22**(2), 127–146 (2014).

[32] Tibaldi, A., Gonzalez Montoya, J. A., Vallone, M., Goano, M., Bellotti, E., and Bertazzi, F., "Modeling infrared superlattice photodetectors: From nonequilibrium Green's functions to quantum-corrected drift diffusion," *Phys. Rev. Appl.* **16**, 044024 (Oct. 2021).

[33] Vallone, M., Goano, M., and Tibaldi, A., "High operating temperature HgCdTe coupled cavity plasmonic infrared photodetectors," *Opt. Express* **32**(16), 27536–27551 (2024).

[34] Vallone, M., Tibaldi, A., Hanna, S., Wegmann, A., Eich, D., Figgemeier, H., Bertazzi, F., Ghione, G., and Goano, M., "Plasmon-enhanced light absorption in mid-wavelength infrared HgCdTe detectors," *IEEE J. Select. Topics Quantum Electron.* **28**, 3802310 (Mar./Apr. 2022).

[35] Yariv, A. and Yeh, P., [*Photonics: optical electronics and modern communications*], Oxford Univ. Press, New York, 6th ed. (2007).

[36] Vanamala, N., Santiago, K. C., Das, N. C., and Hargrove, S. K., "Geometric optimization of plasmonic nanostructure arrays on MWIR HgCdTe (MCT)," *AIP Adv.* **10**, 065006 (2020).

[37] Born, M. and Wolf, E., [*Principles of Optics. Electromagnetic Theory of Propagation, Interference and Diffraction of Light*], Cambridge University Press, Cambridge, U.K., 7th ed. (1999).

[38] Synopsys, Inc., Optical Solutions Group, Ossining, NY, *RSoft FullWAVE User Guide, v2019.09* (2019).

[39] Jackson, J. D., [*Classical Electrodynamics*], Wiley, New York, USA, 3rd ed. (1999).

[40] Orfanidis, S. J., "Electromagnetic waves and antennas." `https://www.ece.rutgers.edu/~orfanidi/ewa/` (2016).

[41] Keasler, C. and Bellotti, E., "Three-dimensional electromagnetic and electrical simulation of HgCdTe pixel arrays," *J. Electron. Mater.* **40**(8), 1795–1801 (2011).

[42] Liang, J., Hu, W., Ye, Z., Liao, L., Li, Z., Chen, X., and Lu, W., "Improved performance of HgCdTe infrared detector focal plane arrays by modulating light field based on photonic crystal structure," *J. Appl. Phys.* **115**(18), 184504 (2014).

[43] Vallone, M., Goano, M., Bertazzi, F., Ghione, G., Schirmacher, W., Hanna, S., and Figgemeier, H., "Comparing FDTD and ray tracing models in the numerical simulation of HgCdTe LWIR photodetectors," *J. Electron. Mater.* **45**(9), 4524–4531 (2016).

[44] Vallone, M., Goano, M., Bertazzi, F., Ghione, G., Schirmacher, W., Hanna, S., and Figgemeier, H., "Simulation of small-pitch HgCdTe photodetectors," *J. Electron. Mater.* **46**(9), 5458–5470 (2017).

[45] Hougen, C. A., "Model for infrared absorption and transmission of liquid-phase epitaxy $\mathrm{Hg}_{1-x}\mathrm{Cd}_x\mathrm{Te}$," *J. Appl. Phys.* **66**(8), 3763–3766 (1989).

[46] Capper, P. and Garland, J., eds., [*Mercury Cadmium Telluride. Growth, Properties and Applications*], John Wiley & Sons, Chichester, U.K. (2011).

[47] Ordal, M. A., Long, L. L., Bell, R. J., Bell, S. E., Bell, R. R., Alexander, R. W., and Ward, C. A., "Optical properties of the metals Al, Co, Cu, Au, Fe, Pb, Ni, Pd, Pt, Ag, Ti, and W in the infrared and far infrared," *Appl. Opt.* **22**(7), 1099–1119 (1983).

[48] Vasileska, D., Goodnick, S. M., and Klimeck, G., [*Computational Electronics. Semiclassical and Quantum Device Modeling and Simulation*], CRC Press, Boca Raton, FL (2010).

[49] Synopsys, Inc., Mountain View, CA, *Sentaurus Device User Guide. Version N-2017.09* (Sept. 2017).

[50] Goano, M., Bertazzi, F., Zhou, X., Mandurrino, M., Dominici, S., Vallone, M., Ghione, G., Tibaldi, A., Calciati, M., Debernardi, P., Dolcini, F., Rossi, F., Verzellesi, G., Meneghini, M., Trivellin, N., De Santi, C., Zanoni, E., and Bellotti, E., "Challenges towards the simulation of GaN-based LEDs beyond the semiclassical framework," in [*SPIE Photonics West. Physics and Simulation of Optoelectronic Devices XXIV*], **9742, Proceedings of the SPIE**, 974202 (Feb. 2016).

[51] Vallone, M., Mandurrino, M., Goano, M., Bertazzi, F., Ghione, G., Schirmacher, W., Hanna, S., and Figgemeier, H., "Numerical modeling of SRH and tunneling mechanisms in high-operating-temperature MWIR HgCdTe photodetectors," *J. Electron. Mater.* **44**(9), 3056–3063 (2015).

[52] Lopes, V. C., Syllaios, A. J., and Chen, M. C., "Minority carrier lifetime in mercury cadmium telluride," *Semiconductor Sci. Technol.* **8**, 824–841 (June 1993).

[53] Kinch, M. A., Aqariden, F., Chandra, D., Liao, P.-K., Schaake, H. F., and Shih, H. D., "Minority carrier lifetime in *p*-HgCdTe," *J. Electron. Mater.* **34**(6), 880–884 (2005).

[54] Su, J., Li, C., Xiao, J., Kong, J., Hu, P., Lu, C., and Zhu, L., "Boosting infrared absorption through surface plasmon resonance enhanced HgCdTe microcavity," *J. Appl. Phys.* **134**, 243106 (2023).

[55] Alasio, M. G. C., Vallone, M., Tibaldi, A., Namnabat, S., Adams, D., Gothoskar, P., Forghieri, F., Masini, G., Bertazzi, F., Ghione, G., Gioannini, M., and Goano, M., "TCAD-assisted progress on the CISCO platform towards low-bias 200 Gbit/s vertical-*pin* Ge-on-Si waveguide photodetectors," *J. Lightwave Technol.* **42**, 1–8 (Jan. 2024).